ChemPubSoc Europe

DOI: 10.1002/cssc.201902232

CHEMSUSCHEM Full Papers

Metal–Organic Framework-Derived Fe/Co-based Bifunctional Electrode for H_2 Production through Water and Urea Electrolysis

Thangjam Ibomcha Singh,[a] Gaddam Rajeshkhanna,[a] Soram Bobby Singh,[a] Tolendra Kshetri,[a] Nam Hoon Kim,*[a] and Joong Hee Lee*[a, b]

Hollow-structured $Fe_xCo_{2-x}P$, $Fe_xCo_{3-x}O_4$, and Prussian blue analogue (FeCo-PBA) microbuilding arrays on Ni foam (NF) are derived from Co-based metal–organic frameworks (Co-MOF) using a simple room temperature and post-heat-treatment route. Among them, $Fe_xCo_{2-x}P$/NF shows excellent bifunctional catalytic activities by demonstrating very low oxygen evolution reaction (OER) and hydrogen evolution reaction (HER) overpotentials of 255/114 mV at a current density of 20/10 mA cm^{-2} respectively, whereas $Fe_xCo_{3-x}O_4$/NF and FeCo-PBA/NF demand higher overpotentials. Remarkably, for water electrolysis, $Fe_xCo_{2-x}P$/NF requires only 1.61 V to obtain 10 mA cm^{-2}. In contrast to water electrolysis, urea electrolysis reduces overpotential and simultaneously purifies the urea-rich wastewater. The urea oxidation reaction at the $Fe_xCo_{2-x}P$/NF anode needs just 1.345 V to achieve 20 mA cm^{-2}, which is 140 mV less than the 1.48 V potential required for OER. Moreover, the generation of H_2 through urea electrolysis needs only 1.42 V to drive 10 mA cm^{-2}.

Introduction

Electrochemical water splitting is a simple, convenient, and promising approach to produce H_2 fuel, which can avoid the risk of environmental pollution and energy crisis.[1,2] However, the sustainable, large scale production of H_2 through electrochemical water splitting has been limited over the years by the sluggish kinetics of its half-cell reactions, high cost, and scarcity of the state-of-the-art electrocatalysts (i.e., RuO_2, IrO_2, and Pt-based catalysts).[3,4] This is the driving force for the development of high-efficiency and inexpensive electrocatalysts to enhance the sluggish oxygen evolution reaction (OER) and hydrogen evolution reaction (HER) as well as to replace the noble metals. The significant developments of electrocatalysts for each half-cell reaction for OER are transition metal-based layered double hydroxides,[5,6] (oxy)hydroxides,[7,8] and oxides;[9–13] whereas for HER, they are typically phosphides,[14,15] chalcogenides,[16,17] and carbides.[18,19] However, the development of an effective bifunctional (i.e., active for OER and HER) electrocatalyst for overall water electrolysis in the same electrolyte is currently challenging and quite limited, especially in alkaline media owing to the pH sensitivity of the electrocatalysts. Therefore, to meet the requirements for sustainable water splitting, new materials and new synthesis strategies need to be explored to obtain novel electrocatalysts.

Recently, metal–organic frameworks (MOFs) and their derived nanomaterials, such as metal oxides, phosphides, sulfides, and selenides, are explored for OER[20–24] and HER,[25–28] owing to their rich chemical functionalities and tuneable structures with large specific surface areas. However, the exploitation of MOFs and MOFs-derived materials for overall water splitting is still scarce and requires innovative tactics. Among the various transition-metal-based MOFs, Co-based pristine MOFs and their derivatives, such as Co_3O_4, Co_2P, and CoS, are emerging as promising candidates for electrocatalytic applications, owing to the presence of variable oxidation states ($Co^{2+} \leftrightarrow Co^{3+} \leftrightarrow Co^{4+}$), low cost, ease of synthesis, high specific surface area, abundant porosity, and high catalytic activities.[29–33] The recent studies consider metal phosphides to be a new class of highly effective bifunctional electrocatalysts for overall electrochemical water splitting, because of the presence of proton trapping "P" species that serves as a base for HER and also facilitates OER by enhancing the formation of peroxide intermediate.[34] However, most of the reported phosphide catalysts are still insufficient as they consist of simple configuration and morphological features derived from the single metal MOF crystals. Moreover, they are mostly in powder form, which requires a pre-coating process using catalytically inactive polymer binders for their electrocatalytic evaluations, lowering their true electrocatalytic activities by blocking the active sites of the electrocatalysts; the binders are also liable to peel off easily during

[a] T. I. Singh, Dr. G. Rajeshkhanna, Dr. S. B. Singh, Dr. T. Kshetri, Prof. N. H. Kim, Prof. J. H. Lee
Advanced Materials Institute of BIN Convergence Technology (BK21 Plus Global)
Deptartment of BIN Convergence Technology
Jeonbuk National University
Jeonju, Jeonbuk, 54896 (Korea)
E-mail: nhk@jbnu.ac.kr
jhl@jbnu.ac.kr

[b] Prof. J. H. Lee
Carbon Composite Research Centre
Department of Polymer Nano Science and Technology
Jeonbuk National University
Jeonju, Jeonbuk, 54896 (Korea)

Supporting Information and the ORCID identification number(s) for the author(s) of this article can be found under: https://doi.org/10.1002/cssc.201902232.

rapid gas evolution.[35,36] Therefore, the development of free-standing MOF composites to enhance their electrocatalytic activities by integrating multiple metal compositions on conducting substrates, such as metal foil, metal foam, and carbon cloth, is highly necessary.

MOFs are also excellent candidates for the preparation of various kinds of hollow-structured materials, which can enhance the electrocatalytic activities by allowing the easy diffusion of molecules/ions and shortening of the ion transport path. Recently, Lou and co-workers have developed a variety of hollow-structured metal-based nanomaterials from a variety of MOF precursors, and found that they are very active for electrochemical energy conversions and energy storage applications.[21,37–39] However, the development of free-standing hollow-structured MOF-derived materials on conducting 3D metal foams is quite difficult and challenging, and does not necessarily align with the sought-after simple and cost-effective room temperature (RT) synthesis route. In this regard, obtaining MOF-derived materials by ion exchange is an effective route, and it is essential to induce many interesting properties and avoid the intrinsic chemical instability of MOFs.[40] The structural and compositional transformation of nanomaterials by ion exchange using solid–liquid, solid–gas, and solid–solid phase brings out many benefits for electrocatalytic applications.[40–42] However, reports on such a synthesis route are very limited.

To reduce the thermodynamic potential of water electrolysis ($2H_2O \rightarrow 2H_2 + O_2$, $\Delta E^0 = 1.23$ V), urea electrolysis [$CO(NH_2)_2 + H_2O \rightarrow N_2 + 3H_2 + CO_2$, $\Delta E^0 = 0.37$ V] and other alternative reactions to OER, such as N_2 oxidation, tetrahydroisoquinolines oxidative dehydrogenation, and amine oxidation, have very recently been studied for large-scale H_2 production.[43–50] Urea electrolysis is not only advantageous for H_2 generation, it also purifies the wastewater-containing urea, which is much easier and cheaper compared to previously established urea waste treatment methods, such as urea hydrolysis,[51] biodegradation,[52] chemical oxidation,[53] and adsorptions,[54] as they consume high energy and need costly equipment. However, urea electrolysis needs very active electrocatalysts to overcome the sluggish kinetics of the $6e^-$ transfer process of the complex anodic urea oxidation reaction [$CO(NH_2)_2 + 6OH^- \rightarrow N_2 + CO_2 + 5H_2O + 6e^-$, UOR].

Considering all the challenges, in this work, we developed a binder-free, hollow-structured Prussian blue analogue (FeCo-PBA), $Fe_xCo_{3-x}O_4$, and $Fe_xCo_{2-x}P$ microbuilding arrays on Ni foam (NF) by using solid–liquid, solid–gas, and solid–solid phase routes, respectively. Initially, a microbuilding-structured Co-MOF parent material was synthesized on NF by a simple solution-based synthesis route and was further used for Fe-incorporation and anion exchange. The entire synthesis process does not require any complex instruments or organic solvents, highlighting the simplicity of the process. The introduction of Fe into the Co-MOF owing to the anion exchange reaction enhances the intrinsic properties by introducing more active sites and tuning the ionic and electronic conductivities, thereby augmenting the electrocatalytic activities. The electrochemical studies have shown that $Fe_xCo_{2-x}P$/NF exhibits high OER, HER, and overall water splitting capability compared with $Fe_xCo_{3-x}O_4$/NF and FeCo-PBA/NF, because of the multifunctional properties in a single hybrid composite. $Fe_xCo_{2-x}P$/NF was further investigated for UOR and urea electrolysis and exhibits an extremely low potential for both reactions. The synergistic effect of Fe/Co constituents, highly exposed active sites, high specific surface area (SSA), and hollow structure accelerates the mass and electron transport. Therefore, the synthesized electrodes demonstrated unprecedented catalytic activities with excellent stability.

Results and Discussion

Scheme 1 illustrates the synthesis of FeCo-PBA/NF to $Fe_xCo_{2-x}P$/NF and $Fe_xCo_{3-x}O_4$/NF utilizing Co-MOF/NF as the starting material.

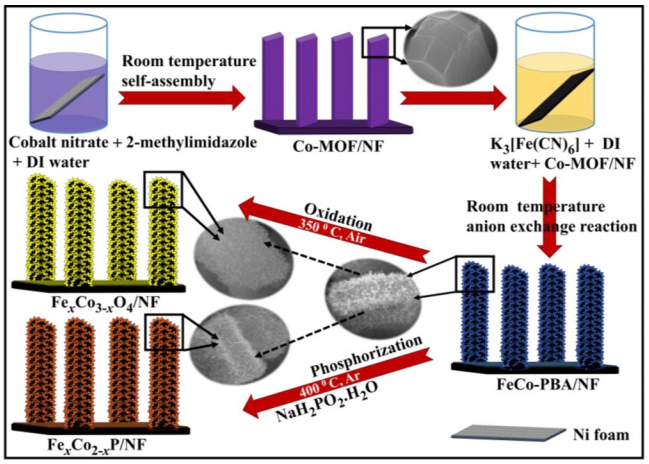

Scheme 1. Synthesis of FeCo-PBA/NF utilizing Co-MOF/NF as the starting material and subsequent conversion to its oxide and phosphide materials.

The calcination temperatures of 350 °C for oxide conversion and 400 °C for phosphide conversion were chosen from the thermal gravimetric analysis (TGA) curves of FeCo-PBA/NF, which are shown in Figure S1 (in the Supporting Information). The synthesized materials were initially examined by powder X-ray diffraction (PXRD), which is a fundamental analysis tool for studying the structure and phase of the synthesized materials.

Figure 1a shows the PXRD patterns of the synthesized materials. The diffraction patterns of the as-synthesized Co-MOF/NF (Figure 1a) resemble those of ZIF-L.[55,56] To incorporate the Fe into the Co-MOF at RT, Co-MOF/NF is soaked in aqueous $K_3[Fe(CN)_6]$ solution (Scheme 1). The resultant material is subjected to PXRD analysis; the corresponding diffraction pattern is quite identical to the diffraction pattern of $Co_2Fe(CN)_6$ (JCPDS No. 75-0039). This indicates that during the anion exchange process, the 2–methylimidazole ligand is replaced by the $[Fe(CN)_6]^{-3}$ ions, and forms FeCo-PBA/NF. After calcination under air atmosphere, the PXRD pattern of FeCo-PBA/NF is completely changed and resembles the diffraction pattern of Co_3O_4 (JCPDS No. 42–1457), signifying the successful conver-

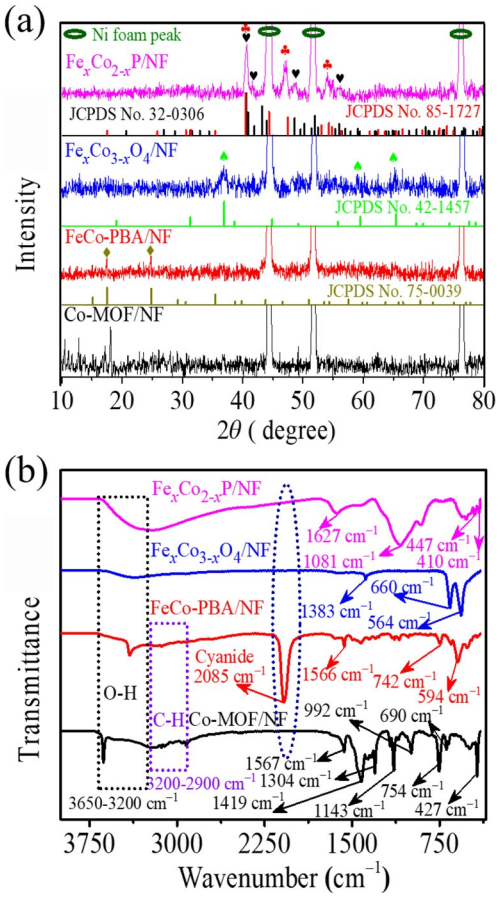

Figure 1. (a) PXRD patterns and (b) FTIR spectra of Co-MOF/NF, FeCo-PBA/NF, $Fe_xCo_{3-x}O_4$/NF, and $Fe_xCo_{2-x}P$/NF.

sion of FeCo-PBA/NF to $Fe_xCo_{3-x}O_4$/NF. Similarly, the diffraction pattern of FeCo-PBA/NF after phosphorization is changed, and it shows distinctly different from the parent materials (Figure 1a). The resultant diffraction peaks at the 2θ values of 40.72, 47.14, 48.62, 51.77, and 53.96° are very close to the binary phosphide phases of orthorhombic Co_2P (JCPDS No. 32–0306) and hexagonal Fe_2P (JCPDS No. 85-1727). This indicates the successful conversion of FeCo-PBA/NF to $Fe_xCo_{2-x}P$/NF. Thus, Co-MOF/NF, FeCo-PBA/NF, $Fe_xCo_{3-x}O_4$/NF, and $Fe_xCo_{2-x}P$/NF materials were synthesized and identified by PXRD. The originated sharp high peaks at 2θ values of 44, 51, and 76° correspond to NF.

Fourier-transform (FT)IR spectroscopy is another essential technique that identifies the surface functional groups and the types of bonding. Figure 1b shows the FTIR spectra of all the samples. The IR bands of Co-MOF are almost similar to the IR bands of ZIF-8 reported previously.[57,58] The bands in the region of 3650–3200 cm^{-1} are attributed to O–H stretching vibrations. A sharp band at approximately 3650 cm^{-1} for Co-MOF corresponds to free O–H stretching vibration. After the anion exchange reaction, the corresponding peak shifted to a lower frequency, owing to the intermolecular bonded O–H stretching vibration. After converting it to the oxide ($Fe_xCo_{3-x}O_4$), the O–H stretching vibration peak was almost disappeared, and a weak broad peak was observed for $Fe_xCo_{2-x}P$ because of the adsorbed water molecules. The IR absorption bands in the region approximately 3200–2900 cm^{-1} can be ascribed to C–H stretching vibration. The observed bands within this region even after the anion exchange reaction signify the presence of a minute amount of imidazole ligand at the core part of the FeCo-PBA material. Meanwhile, $Fe_xCo_{3-x}O_4$ and $Fe_xCo_{2-x}P$ did not show any such bands, indicating the complete decomposition of the imidazole ligand under heat treatment. The strong absorption band at approximately 2085 cm^{-1} for FeCo-PBA/NF corresponds to C≡N, which clearly indicates that the imidazole ligand is exchanged with the cyanide during ligand exchange process at RT. After converting FeCo-PBA to $Fe_xCo_{3-x}O_4$ and $Fe_xCo_{2-x}P$ (represented by a dotted line), the cyanide absorption band disappeared, which further confirms the formation of oxide and phosphide after heat treatment in the presence of air and Ar gas (with sodium hypophosphite), respectively. The peaks within the region 1500–1000 cm^{-1} for Co-MOF and FeCo-PBA materials result from C–H and O–H bending, and C–N stretching vibrations. The observed peaks below approximately 1000 cm^{-1} could be C=C bending vibrations. The IR band at approximately 1627 cm^{-1} for $Fe_xCo_{2-x}P$ corresponds to C=C stretching vibrations, which could result from the presence of the carbon network. This indicates the co-existence of carbon along with $Fe_xCo_{2-x}P$; under heat treatment in the presence of Ar gas, the leftover imidazole and cyanide are expected to decompose and form the N-doped carbon. The peak at approximately 1383 cm^{-1} for $Fe_xCo_{3-x}O_4$ corresponds to O–H stretching.

Field emission scanning electron microscopy (FESEM) is used to investigate the surface morphological features of all the samples. The low and high magnification FESEM images of the starting material (i.e., Co-MOF/NF) show microbuilding-like morphology (Figure S2a), which is vertically grown uniformly on porous 3D NF. The width and thickness of the microbuildings are approximately 0.7 and 0.5 μm, whereas the height/length are approximately a few micrometers (inset of Figure S2a). Figure 2a,b shows the high magnification FESEM images of FeCo-PBA/NF; after the anion-exchange reaction, the uniform and smooth surface of Co-MOF/NF microbuildings are transformed to a rough surface with large porosity. The high-magnification FESEM image (Figure 2b) shows spike-like nanostructures that cover the entire surface of the microbuildings, and also shows that the thickness of the microbuildings is reduced to approximately 200–300 nm (Figure 2b) from approximately 0.5 μm thickness of the Co-MOF microbuildings (Figure S2a). This could be a result of the change in crystal structure and a higher rate of anion exchange. Figure 2c shows the elemental color mapping, which confirms the presence and uniform distribution of Fe, Co, C, N, and O elements. Here, it is interesting to note that the microbuilding-like morphology is retained, even after the anionic ligand exchange. Thus, the RT synthesis of FeCo-PBA/NF not only reduces the cost and complexity, it also allows its original morphology to be retained. In addition, optimizing synthesis conditions and finding a suitable amount of foreign element incorporation are essential criteria for any synthetic strategy. Therefore, FeCo-PBA/NF was synthesized with three different amounts of

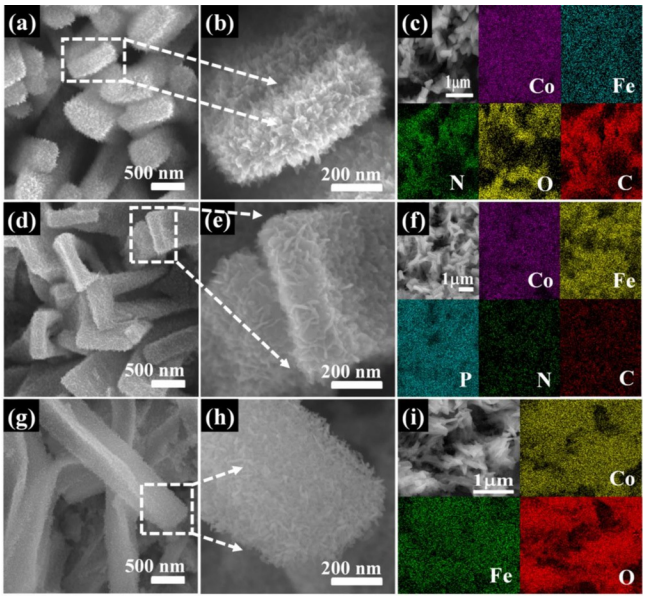

Figure 2. High magnification FESEM images and elemental color mappings of (a–c) FeCo-PBA/NF, (d–f) $Fe_xCo_{2-x}P$/NF, and (g–i) $Fe_xCo_{3-x}O_4$/NF.

$K_3[Fe(CN)_6]$ precursors (i.e., 0.25, 0.5, and 1 mmol). Figure S3 a–f shows the corresponding FESEM images and energy-dispersive X-ray analysis (EDAX) profiles. All the concentrations (Figure S3 a, c, e) show almost the same morphology; however, the one synthesized with 0.5 mmol is found to be uniform in size and arrangement (Figure S3c), whereas the other material contains a higher degree of agglomeration (Figure S3 a, e). Hence, 0.5 mmol has been taken as the optimum concentration. To further optimize the time, FeCo-PBA/NF was synthesized using 12 and 24 h reaction times; Figures S3 a–f, and S4 a, b show the corresponding FESEM images, respectively. Both the materials display the same morphology. Nevertheless, FeCo-PBA/NF at 12 h has a better arrangement and shows less degree of agglomeration compared with the material synthesized at 24 h. Thus, FeCo-PBA/NF synthesized with 0.5 mmol concentration of $K_3[Fe(CN)_6]$ at 12 h reaction time is used for oxide and phosphide conversion, owing to the more uniform and striking morphological features. The $Fe_xCo_{2-x}P$/NF and $Fe_xCo_{3-x}O_4$/NF materials obtained after calcination under Ar atmosphere in the presence of sodium hypophosphite and under air atmosphere, respectively, retain the initial morphology, which is shown in Figures 2 d, e and 2 g, h, respectively. The elemental color mapping of $Fe_xCo_{3-x}O_4$/NF shows the presence of Fe, Co, and O (Figure 2 i). Interestingly, the elemental color mapping of $Fe_xCo_{2-x}P$/NF indicates the existence of Fe, Co, and P, as well as N and C (Figure 2 f). During the calcination process under Ar atmosphere, the cyanide and leftover imidazole ligands at the core are responsible for the generation of N-doped carbon (N-C).[59] This is advantageous to enhance the conductivity of the sample. Therefore, $Fe_xCo_{2-x}P$/NF containing N-C is expected to show higher electrocatalytic activities. The almost complete retention of the original morphology, even after heat treatment, indicates its greater robustness. Further, after heat treatment, the material on the NF is expected to detach from the NF; in this case, this has not happened (Figure S5 a, b), owing to the slow heating rate (1 °C min^{-1}). It should be emphasized here that the RT synthesis and the following heat treatment strategy for oxide and phosphide conversion are deal for the conversion of MOF-based materials to oxides and phosphides.

The in-depth structural-related information of Co-MOF/NF, FeCo-PBA/NF, $Fe_xCo_{2-x}P$/NF, and $Fe_xCo_{3-x}O_4$/NF are investigated by high-resolution transmission electron microscopy (HRTEM) analysis (Figures S6 and 3). Figure S6 shows the HRTEM image, high-angle annular dark-field scanning transmission electron microscopy (HAADF-STEM) image, selected area electron diffraction (SAED) pattern, and energy dispersive X-ray (EDX) spectrum of Co-MOF/NF, confirming its smooth surface and the microbuilding-like structure in agreement with the FESEM images (Figure S2 a). However, after the anion exchange reaction, there is a significant transformation in the internal structure of FeCo-PBA/NF and its oxide and phosphide derivatives. Figure 3 shows low and high magnification HRTEM images, HAADF-STEM images, SAED patterns, and elemental color mappings of FeCo-PBA/NF, $Fe_xCo_{2-x}P$, and $Fe_xCo_{3-x}O_4$, respectively. Figure 3 a shows a typical core–shell like structure, which suggests that FeCo-PBA/NF undergoes partial anion exchange reaction, resulting in the formation of FeCo-PBA as the shell and the leftover interior Co-MOF as the core material. The existence of leftover Co-MOF at the core even after 12 h of anion exchange reaction may be because of the restriction of $[Fe(CN)_6]^{-3}$ anions diffusion by the in situ developed FeCo-PBA layers similar to the previous report.[21] This is also identified by the occurrence of a weak C–H stretching band as discussed in the FTIR spectra of FeCo-PBA/NF. Nonetheless, such partially substituted materials present unique functionalities owing to

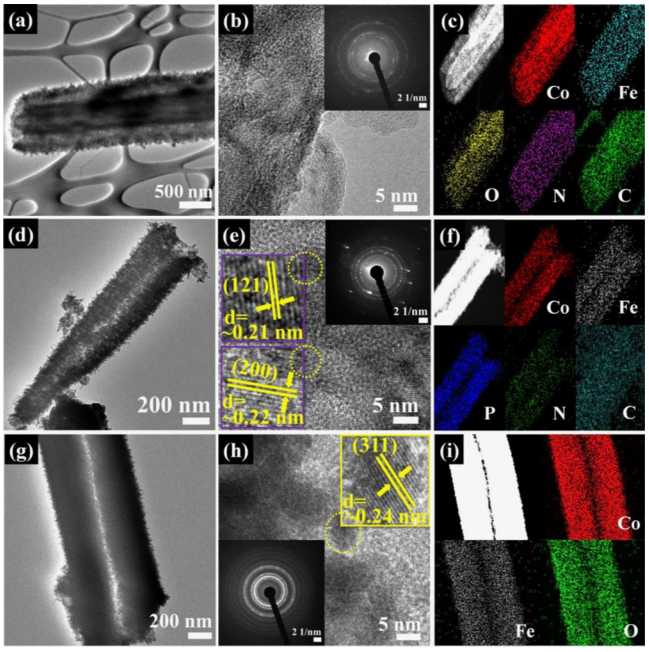

Figure 3. (a, d, g) Low-magnification HRTEM images, (b, e, h) high-magnification HRTEM images (inset: SAED diffraction patterns), and (c, f, i) HAADF-STEM images (first images of c, f, i) and elemental color mappings of (a–c) FeCo-PBA/NF, (d–f) $Fe_xCo_{2-x}P$/NF, and (g–i) $Fe_xCo_{3-x}O_4$/NF.

its multi-component nature and they usually maintain their parent MOF network skeleton. As a result, electrocatalysts derived from such partially substituted materials are expected to exhibit high structural stability and electrocatalytic performances. Interestingly, $Fe_xCo_{2-x}P$/NF and $Fe_xCo_{3-x}O_4$/NF derived from FeCo-PBA/NF consist of hollow structures (Figure 3d, g). The high magnification HRTEM image of $Fe_xCo_{2-x}P$ shows resolved lattice spacings at 0.21 and 0.22 nm, that correspond to (121) and (200) planes of Co_2P and Fe_2P, respectively (inset of Figure 3e). These results agree with the XRD pattern of $Fe_xCo_{2-x}P$/NF. The high magnification HRTEM image of $Fe_xCo_{3-x}O_4$ shows an interlayer spacing of 0.24 nm, that corresponds to (311) plane of Co_3O_4 (Figure 3h). Further, the SAED patterns of all the three materials (inset of Figures 3b, e, h) show circular ring patterns with bright dots, indicating their polycrystalline nature. Figures 3c, f, i show the elemental composition and spatial elemental distribution of FeCo-PBA/NF, $Fe_xCo_{2-x}P$, and $Fe_xCo_{3-x}O_4$, respectively. Figure 3c shows the elemental mapping for FeCo-PBA/NF that indicates the existence of Co, Fe, O, N, and C as the constituent elements and confirms Fe incorporation induced by the anion exchange process. The elemental color mappings of $Fe_xCo_{2-x}P$ shows the presence of Fe, Co, P, C, and N; these elements are evenly distributed over the hollow-microbuilding-like structure, as shown in Figure 3f. Similarly, Figure 3i confirms the presence of Fe, Co, and O for $Fe_xCo_{3-x}O_4$. These results further support the FESEM observations. The high contrast bright images (first images of Figure 3c, f, i) of the materials also confirm the hollow structure, which is indicated by the dark linear regions in the microbuilding-like structure. The hollow structure is another advantage for these materials as it improves catalytic activities by allowing a large number of electrolyte ions/molecules accessible and makes the entire electrode material active. In particular, $Fe_xCo_{2-x}P$ is expected to exhibit higher electrochemical activity owing to the hollow structure, as well as to consist of high conductivity N-C.

The SSA and the pore size of the material are two important factors that influence the electrocatalytic activities. Therefore, to evaluate the SSA and the pore size distribution of Co-MOF, FeCo-PBA, $Fe_xCo_{3-x}O_4$, and $Fe_xCo_{2-x}P$, we have recorded the N_2 adsorption-desorption isotherms. Figure S7a–d shows the Brunauer–Emmett–Teller (BET) N_2 sorption isotherms of Co-MOF, FeCo-PBA, $Fe_xCo_{3-x}O_4$, and $Fe_xCo_{2-x}P$, respectively. The N_2 sorption isotherm of Co-MOF demonstrates a typical Type I isotherm curve (Figure S7a), whereas the other three show typical Type IV isotherm curves (Figure S7b–d). The Barret–Joyner–Halenda (BJH) pore size distribution profiles of FeCo-PBA, $Fe_xCo_{3-x}O_4$, and $Fe_xCo_{2-x}P$ (insets of Figure S7b–d) show the mesoporosity with the pore radii in the range of 5–10 nm, whereas the BJH pore size distribution curve of Co-MOF (inset of Figure S7a) shows the microporous nature with a pore radius below approximately 2 nm. The estimated BET SSA of Co-MOF, FeCo-PBA, $Fe_xCo_{3-x}O_4$, and $Fe_xCo_{2-x}P$ samples are 69.11, 89.61, 96.45, and 118.41 $m^2 g^{-1}$, respectively. The highest SSA of $Fe_xCo_{2-x}P$ compared to other materials is a result of the controlled decomposition of the organic components upon heat treatment during the phosphorization process.

X-ray photoelectron spectroscopy (XPS) was used to study the near-surface chemical compositions and the oxidations states of the constituents of FeCo-PBA/NF, $Fe_xCo_{3-x}O_4$/NF, and $Fe_xCo_{2-x}P$/NF; Figures S8, S9, and 4 show the corresponding XPS spectra, respectively. The wide scan survey spectrum of $Fe_xCo_{2-x}P$/NF confirms the presence of Co, Fe, N, C, P, and O as the constituent elements (Figure 4a). The deconvoluted Co 2p XPS spectrum of $Fe_xCo_{2-x}P$/NF (Figure 4b) shows peaks at binding energy (BE) values of 797.7 and 793.8 eV, which correspond to the spin-orbit splitting values of Co $2p_{3/2}$.[42,60] The resultant peaks at 781.6 and 779 eV correspond to the spin-orbit splitting value of Co $2p_{1/2}$.[42,61,62] The satellite peaks at 784.6 and 802.7 eV for Co $2p_{3/2}$ and Co $2p_{1/2}$, respectively, are characteristic peaks of the Co 2p spectrum.[42] The weak peak at 773.5 eV could correspond to the lower oxidation state of Co ($Co^{\delta+}$), which could be a result of the weaker electronegativity of P. The deconvoluted high-resolution Fe 2p spectrum (Figure 4c) shows main peaks of Fe_2P at 713.3 and 724.6 eV, that are attributed to the Fe $2p_{3/2}$ and Fe $2p_{1/2}$ electronic configurations, respectively.[63] The satellite peaks positioned at 718.0 and 735.3 eV signify the co-occurrence of Fe^{2+} and Fe^{3+} species,[42,62] whereas a peak at 707.4 eV could be the result of the lower oxidation state of the Fe ($Fe^{\delta+}$), which is balanced with the low-coordinated metal-phosphide structure.[64] Figure 4d shows the deconvoluted P 2p XPS spectrum, where the two peaks at 129.0 and 129.86 eV correspond to the characteristic spin-orbit peaks of P $2p_{3/2}$ and P $2p_{1/2}$, respectively.[42] The peaks at BE of 132.5 and 133.5 eV are attributed to the oxidized P, owing to the air exposure.[65] The N 1s XPS spectrum (Figure 4e) shows three distinct peaks at BE of 400.8, 399.8, and 398.8 eV, which correspond to three different types of N configurations such as pyrrolic-N, nitrile-N, and pyridinic-N, respectively.[66] The deconvolution of high resolution C 1s spectrum also shows three peaks: the BE of 288.1 eV corresponds to C=O, a peak at 285.5 eV corresponds to C–N, and the other peak at 284.4 eV corresponds to sp^2 carbon (Figure 4f).[66] This confirms the presence of N-doped carbon, along with $Fe_xCo_{2-x}P$. These findings agree with the microscope elemental color mappings of the $Fe_xCo_{2-x}P$ sample (Figure 2f and 3f), indicating the reliable elemental composition of the prepared material. Similarly, the survey spectrums and deconvoluted constituents XPS spectra of the FeCo-PBA/NF (Figure S8), and $Fe_xCo_{3-x}O_4$/NF (Figure S9) materials confirm the presence of the associated elements.

Electrochemical Studies

Electrocatalytic study for OER

OER is assumed to be the bottleneck for overall water splitting. Therefore, the OER catalytical activity of FeCo-PBA/NF, $Fe_xCo_{3-x}O_4$/NF, and $Fe_xCo_{2-x}P$/NF electrodes were first measured using a typical three-electrode system in an aqueous 1.0 M KOH electrolyte. Before taking the actual measurements, all three electrodes were stabilized by recording 100 non-stop cyclic voltammetry (CV) cycles at a scan rate of 20 $mV s^{-1}$. Figure 5a shows the *iR*-corrected linear sweep voltammetry (LSV)

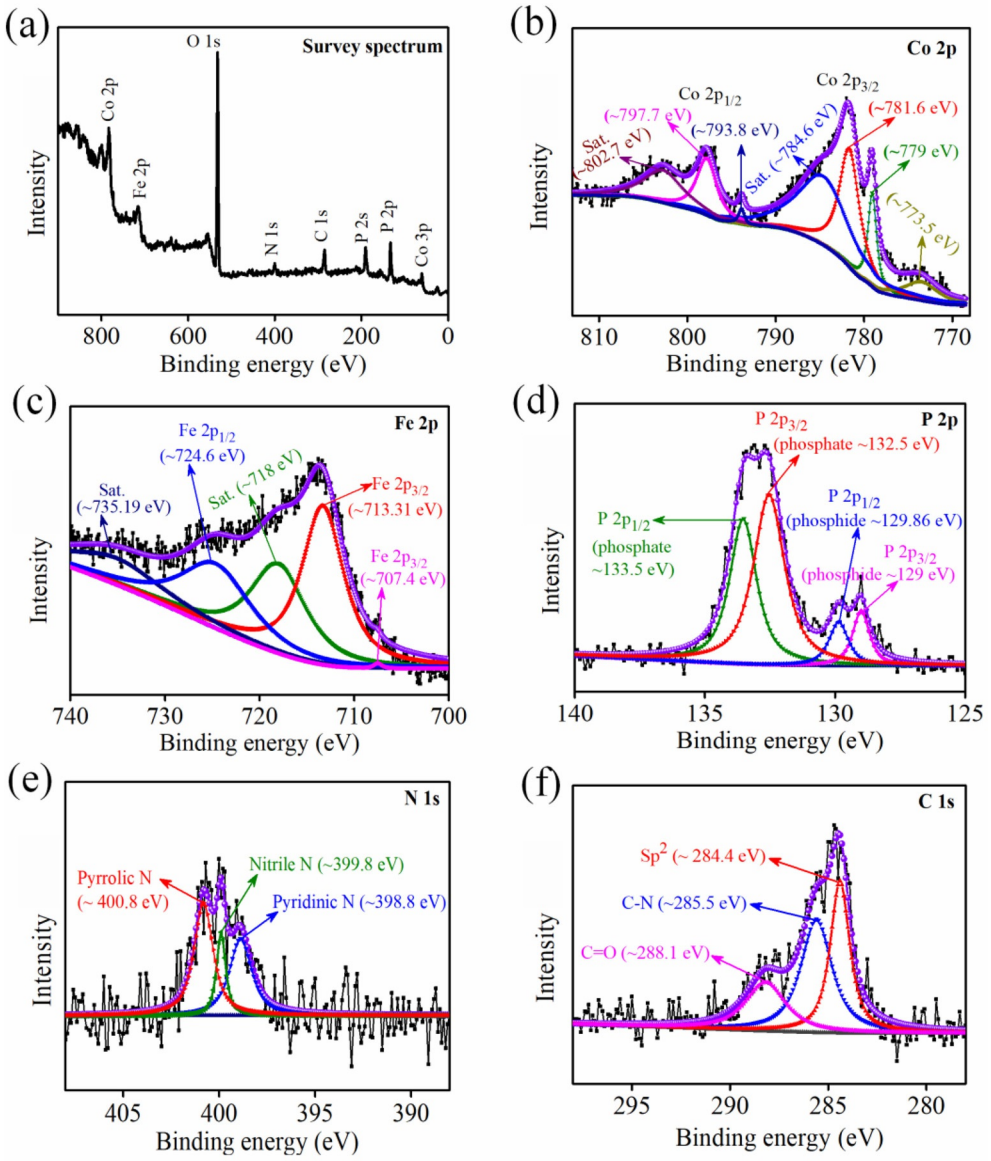

Figure 4. XPS analysis of $Fe_xCo_{2-x}P$/NF (a) survey spectrum and the deconvoluted spectra of (b) Co 2p, (c) Fe 2p, (d) P 2p, (e) N 1s, and (f) C 1s.

curves of FeCo-PBA/NF, $Fe_xCo_{3-x}O_4$/NF, and $Fe_xCo_{2-x}P$/NF electrodes for OER at a scan rate of 2 mV s^{-1} on the reversible hydrogen electrode (RHE). The estimated overpotentials (η) according to the equation $\eta = E_{RHE} - 1.23$ V at a current density of 20 mA cm^{-2} for FeCo-PBA/NF, $Fe_xCo_{3-x}O_4$/NF, and $Fe_xCo_{2-x}P$/NF electrodes are 362, 327, and 255 mV, respectively. For comparison, the LSV curves of the state-of-the-art RuO_2/NF catalyst and bare NF are also recorded at the same scan rate, and the η of these materials are 360 and 387 mV, respectively. These η are significantly higher than the values of the synthesized materials. Among them, $Fe_xCo_{2-x}P$/NF shows the lowest η. The estimated η of FeCo-PBA/NF, $Fe_xCo_{3-x}O_4$/NF, $Fe_xCo_{2-x}P$/NF, RuO_2/NF, and bare NF at 50 mA cm^{-2} are 387, 350, 273, 430, and 446 mV, respectively. At all other current densities also, the $Fe_xCo_{2-x}P$/NF materials show the lowest η compared with the other materials, and Figure 5 a, b shows the comparison. This signifies that $Fe_xCo_{2-x}P$/NF material shows the highest catalytic activity towards OER. The electrocatalytic performance order at all current densities is FeCo-PBA/NF < $Fe_xCo_{3-x}O_4$/NF < $Fe_xCo_{2-x}P$/NF. Though the η of $Fe_xCo_{3-x}O_4$/NF is higher than $Fe_xCo_{2-x}P$/NF material, it is comparable, and still better than many of the recently studied OER electrocatalysts; Table S1 shows the comparison. This demonstrates that the Fe-incorporated anion exchange strategy at RT is highly useful to derive the high-performance oxide and phosphide materials. For more clear perceptions, Figure 5 c shows the Tafel plots of all the samples that are generated from their corresponding *iR*-corrected LSV curves by using the Tafel equation: $\eta = b \log(j/j_o)$ (where η is overpotential, b is Tafel slope, j is current density, and j_o is exchange current density). Clearly, $Fe_xCo_{2-x}P$/NF electrode exhibits much lower Tafel slope (55 mV dec^{-1}) relative to $Fe_xCo_{3-x}O_4$/NF (57 mV dec^{-1}), FeCo-PBA/NF (66 mV dec^{-1}),

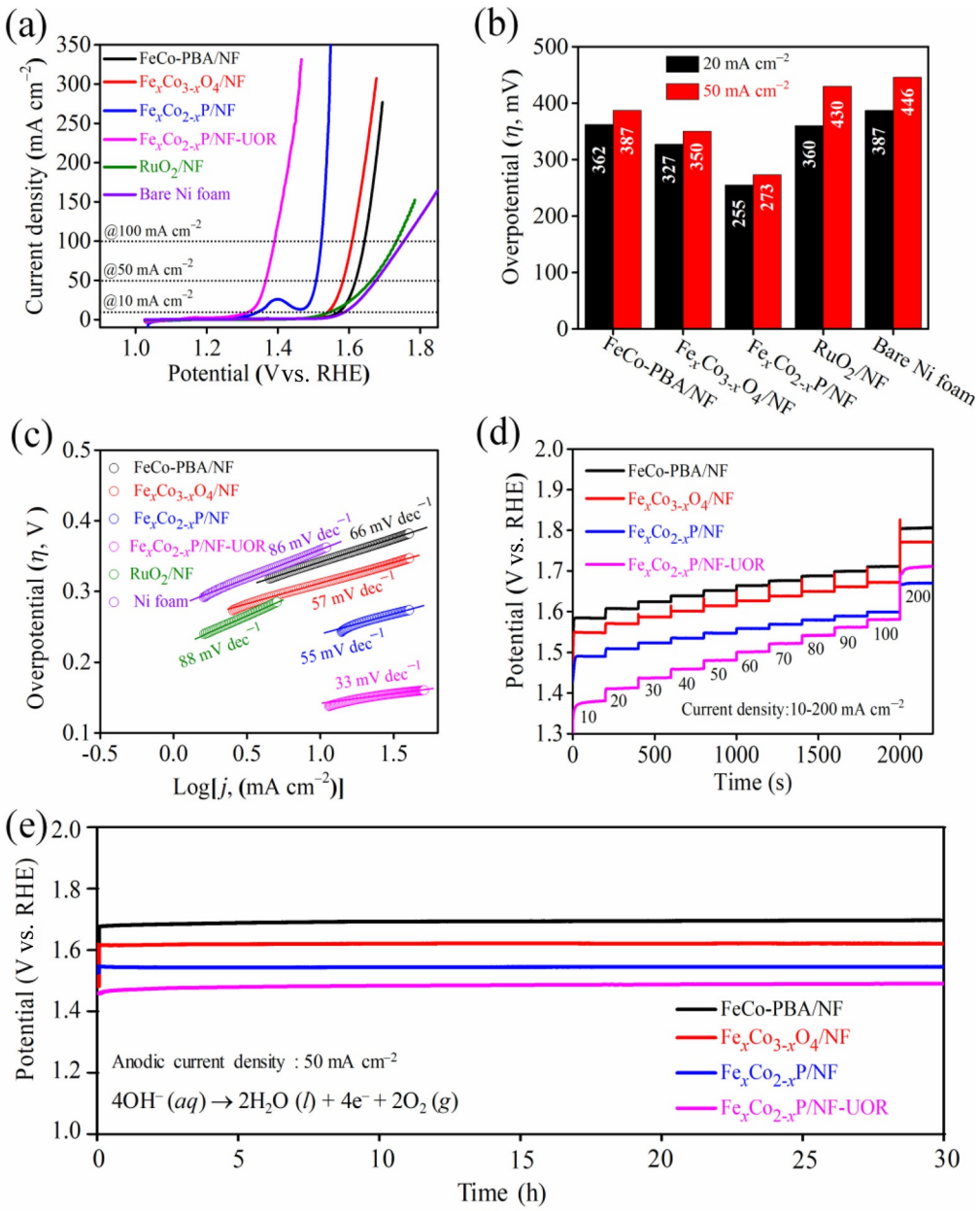

Figure 5. OER/UOR evaluations: (a) *iR* corrected LSV curves at a scan rate of 2 mV s^{-1}, (b) comparison of overpotentials at the current densities of 20 mA cm^{-2} and 50 mA cm^{-2}, (c) tafel plots, (d) multi-current step curves, and (e) chronopotentiometry stability test profiles of FeCo-PBA/NF, $Fe_xCo_{3-x}O_4$/NF, and $Fe_xCo_{2-x}P$/NF electrodes recorded in 1.0 M KOH electrolyte for OER and 1.0 M KOH + 0.5 M urea for UOR.

RuO_2/NF (88 mV dec^{-1}), and bare NF (86 mV dec^{-1}). These findings indicate that the reaction kinetics for $Fe_xCo_{2-x}P$/NF and $Fe_xCo_{3-x}O_4$/NF electrodes are more favorable, further demonstrating their higher OER catalytic activity. Table S1 shows the comparison of the Tafel slopes with the recent reports. The better OER performances of $Fe_xCo_{2-x}P$/NF and $Fe_xCo_{3-x}O_4$/NF in terms of lower overpotential and Tafel slope compared to previously reported electrocatalysts show that materials with hollow structures with high porosity function as efficient catalysts for OER. Besides, some research groups have theoretically and experimentally studied the influence of Fe-doping to the pristine catalysts on the OER performance. They showed that the integration of Fe promotes OER performance by increasing the electrical conductivity, and providing more electroactive metal sites.[67,68] This study shows that in addition to Fe-incorporation, the counter anion is also an important consideration for improving OER catalytic activity. The $Fe_xCo_{2-x}P$/NF and $Fe_xCo_{3-x}O_4$/NF electrodes show the best OER performance compared to the FeCo-PBA/NF, whereas $Fe_xCo_{2-x}P$/NF shows the best catalytic activity compared to the $Fe_xCo_{3-x}O_4$/NF. During the catalytic activities, the electrons present in the metal orbitals take part in bond formation with the adsorbates; therefore, introducing a low electronegative P species can effectively regulate the electronic structure of metal orbi-

tals, and thereby augment the OER performance. The presence of trace amounts of N-C with the $Fe_xCo_{2-x}P$/NF is also responsible for its higher OER performance. The electrochemically active surface area (ECSA) of the electrocatalysts are also determined using the previously established equation ECSA = C_{dl}/C_s [where C_{dl} is the electrochemical double layer capacitance and C_s is the specific capacitance of a flat smooth surface of the electrode material (40 μF cm^{-2})].[69] The obtained C_{dl} values for FeCo-PBA/NF, $Fe_xCo_{3-x}O_4$/NF, and $Fe_xCo_{2-x}P$/NF electrodes are 1.725, 4.13, and 9.625 mF cm^{-2}, respectively (Figure S10). Since the ECSA is directly proportional to C_{dl}, $Fe_xCo_{2-x}P$/NF electrode is found to have the higher ECSA. The higher ECSA of $Fe_xCo_{2-x}P$/NF could be a result of the presence of anionic P species, as well as N-C. Further, to evaluate the quick electrocatalytic response of the electrocatalysts to various current densities with short intervals, multi-current steps profiles are recorded using multi-current steps technique in the current density range 10–200 mA cm^{-2} with a time interval of 200 s, which is shown in Figure 5d. For all the electrodes, at each step, the potential rises with the rise in current density, and at each step, the potential elevates sharply, stabilize quickly, and remains constant for a duration of 200 s. Such behavior is a result of the superb mass-transport property and mechanical stability that enables the movement of hydroxide ions inward and oxygen bubble outward without any disruption throughout the entire current density ranges. The multi-current step profiles also show the lowest potential for $Fe_xCo_{2-x}P$/NF electrode at all current densities, further indicating its superior OER catalytic activity. Along with the lower overpotential, stability for a long duration of time at high current conditions is another important consideration for practical use. Therefore, Figure 5e shows the corresponding plots of the stability of the FeCo-PBA/NF, $Fe_xCo_{3-x}O_4$/NF, and $Fe_xCo_{2-x}P$/NF electrodes, which are evaluated using chronopotentiometry (CP) technique by applying a high anodic current density of 50 mA cm^{-2} for a duration of 30 h. All the materials maintained almost constant potential for 30 h, despite the rapid oxygen evolution caused by the applied high current density. However, throughout the long-term stability, $Fe_xCo_{2-x}P$/NF electrode maintained lower potential, compared with the FeCo-PBA/NF and $Fe_xCo_{3-x}O_4$/NF electrodes. The stability order is FeCo-PBA/NF < $Fe_xCo_{3-x}O_4$/NF < $Fe_xCo_{2-x}P$/NF. Thus, $Fe_xCo_{2-x}P$/NF shows the highest stability, as well as catalytic activity, compared with the other two materials. Figures S11a and S11d show the LSV and multi-current steps profiles, respectively, that were recorded after the CP stability test. After the stability test, both the profiles show an insignificant change in the performance for $Fe_xCo_{2-x}P$/NF electrode, whereas they show slight decay for $Fe_xCo_{3-x}O_4$/NF, and considerable degradation for FeCo-PBA/NF, which follows the trend of overpotential and the Tafel slopes (Figure S11b,c). This indicates that metal phosphides are found to be prominent materials for OER compared to oxides, whereas PBAs are not suited; however, they act as a transition state for the ion exchange process. Further, to check the long-term stability of $Fe_xCo_{2-x}P$/NF, 1000 CV cycles were recorded continuously at the scan rate of 50 mV s^{-1}; afterward, LSV profiles were recorded in the fresh 1 M KOH electrolyte, and compared with the initial one, as shown in Figure S12. After 1000 CV cycles, the overpotential values remain almost the same up to the current density of approximately 100 mA cm^{-2}, and a minimal difference of approximately 5 mV is observed at the higher current density of 200 mA cm^{-2}. Thus, $Fe_xCo_{2-x}P$/NF electrode shows higher OER catalytic activity and operational stability; it requires only 1.50 V (vs. RHE) to generate a high current density of 50 mA cm^{-2}, whereas $Fe_xCo_{3-x}O_4$/NF and FeCo-PBA/NF need potentials of 1.58 and 1.62 V, respectively, for the same current density.

Further, for the energy-saving electrolysis of large-scale H_2 production as well as urea-rich wastewater purification through UOR, urea electrolysis is becoming a hot topic. Therefore, the UOR activity of $Fe_xCo_{2-x}P$/NF ($Fe_xCo_{2-x}P$/NF-UOR) electrode is examined using a three-electrode cell in 1 M KOH containing 0.5 M urea. Figure 5a,d shows the LSV profile and multi-current steps profile, respectively, of $Fe_xCo_{2-x}P$/NF-UOR. They show that in the presence of urea, the overpotentials of $Fe_xCo_{2-x}P$ at all current densities are drastically reduced, owing to the urea oxidation that can significantly decrease the cell potential of the overall water splitting for H_2 production in large scale. The potentials of $Fe_xCo_{2-x}P$/NF-UOR in the presence of urea at current densities of 20 and 50 mA cm^{-2} are 1.345 and 1.367 V (Figure 5a), respectively. These potentials are much lower than the values of 1.485 and 1.508 V for OER at the same current densities, respectively. The derived Tafel slope for the UOR is 33 mV dec^{-1} (Figure 5c), which is significantly lower than the Tafel slope (55 mV dec^{-1}) obtained for the OER. This indicates that the UOR at $Fe_xCo_{2-x}P$/NF electrode has more favorable kinetics compared to OER. Figure 5e shows the CP stability measurement at a current density of 50 mA cm^{-2}, which reveals stable UOR by maintaining almost the initial potential until 30 h. Table S2 shows the UOR performance comparison of $Fe_xCo_{2-x}P$/NF electrode with the recent reports, which indicates its superior UOR activity. This demonstrates that $Fe_xCo_{2-x}P$/NF electrode is a versatile catalyst in terms of catalytic activity and stability. Further, to check the electrocatalytic activity trend of the electrocatalysts with respect to mass loading and ECSA, we have normalized the OER and UOR LSV curves of the electrocatalysts with their corresponding mass loadings and ECSA values, which are shown in Figure S13a,b. In both cases, the electrocatalytic activity trend is similar to that of Figure 5a.

The excellent OER and UOR catalytic activity and stability of $Fe_xCo_{2-x}P$/NF electrode can be assigned to the following motives: (i) highly porous and hollow structured microbuilding-like material can enhance the electrolyte passage, increase wettability, and thereby increase its ECSA; (ii) the hollow structure also favors easy removal of the gas-bubbles produced at the electrode sites during the OER/UOR process; and (iii) the presence of N-C with $Fe_xCo_{2-x}P$/NF enhances intrinsic conductivity; therefore, it shows lower charge transfer resistance (R_{ct} ≈ 0.77 Ω) and solution resistance (R_s ≈ 0.65 Ω), compared to $Fe_xCo_{3-x}O_4$/NF (R_s ≈ 0.68 Ω, R_{ct} ≈ 5.5 Ω) and FeCo-PBA/NF (R_s ≈ 0.82 Ω, R_{ct} ≈ 60.3 Ω; Figure S14).

Electrocatalytic study for HER

The HER activities of $Fe_xCo_{2-x}P$/NF, $Fe_xCo_{3-x}O_4$/NF, and FeCo-PBA/NF are also investigated in the same alkaline electrolyte as that of OER. For comparison, bare NF and state-of-the-art HER catalyst Pt/C/NF are also included in the HER evaluation. Figure 6a shows the *iR*-corrected LSV curves of the prepared catalysts, as well as commercial Pt/C/NF and bare NF, recorded at a scan rate of 2 mV s^{-1}. Figure 6b shows the overpotential comparison at the current densities of 10 and 50 mA cm^{-2}. The hollow-structured $Fe_xCo_{2-x}P$/NF shows the lowest overpotential next to Pt/C/NF, requiring an overpotential of only 114 mV to reach the benchmark current density of 10 mA cm^{-2}, and only 182 mV to achieve a high current density of 50 mA cm^{-2}, compared with $Fe_xCo_{3-x}O_4$/NF (194 and 291 mV), FeCo-PBA/NF (237 and 301 mV), and bare NF (309 and 462 mV) for the same current densities, respectively, as shown in Figure 6b. The superior HER activity of $Fe_xCo_{2-x}P$/NF is further corroborated by the lower Tafel slope of 97 mV dec^{-1} compared to that of $Fe_xCo_{3-x}O_4$/NF (134 mV dec^{-1}) and FeCo-PBA/NF (110 mV dec^{-1}) (Figure 6c). Table S3 compares the HER activities of the prepared electrode materials with the recent literature, which

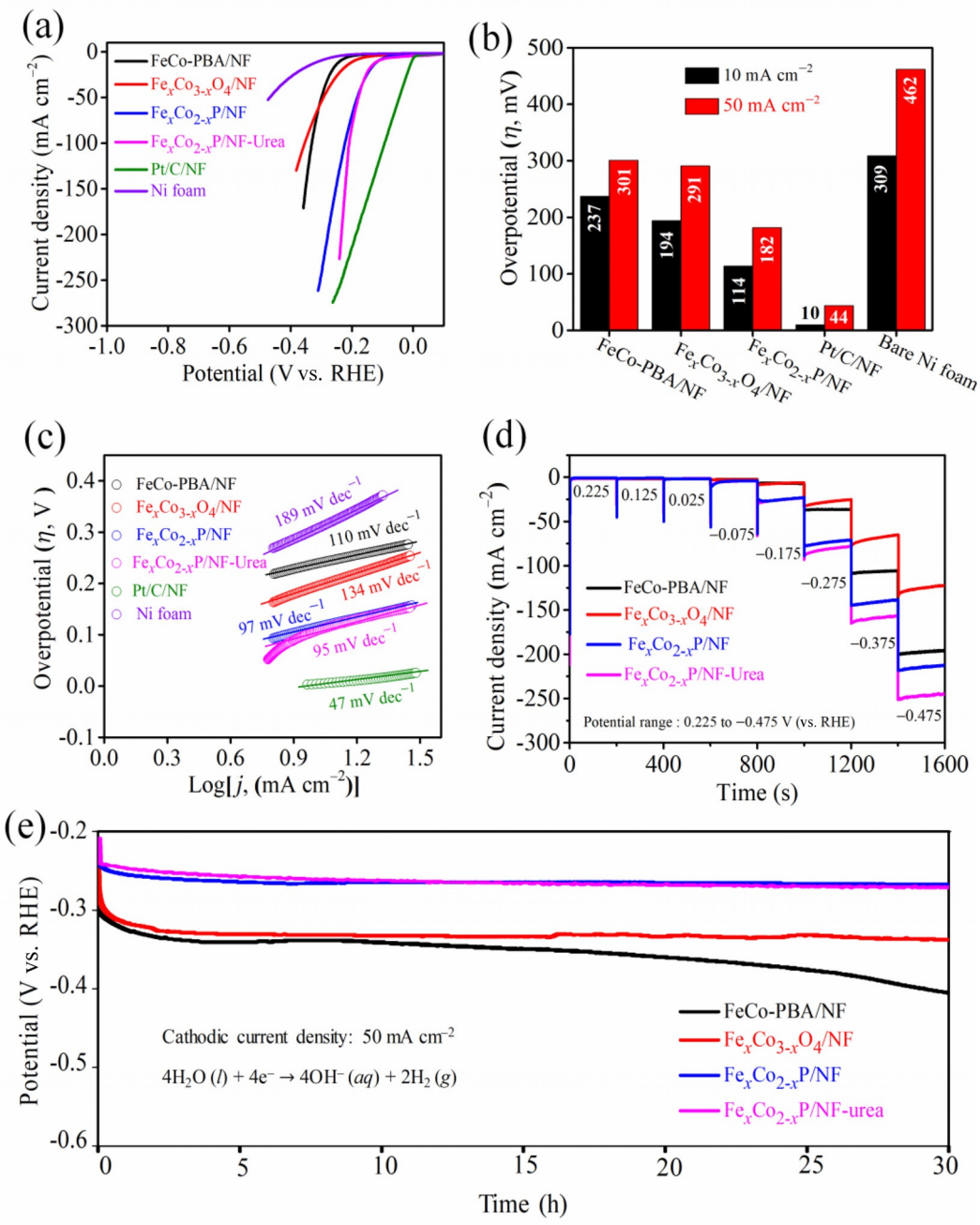

Figure 6. HER evaluations: (a) *iR* corrected LSV curves at a scan rate of 2 mV s^{-1}, (b) comparison of overpotentials at the current densities of 10 and 50 mA cm^{-2}, (c) tafel plots, (d) multi-potential step curves, and (e) chronopotentiometry stability test profiles of FeCo-PBA/NF, $Fe_xCo_{3-x}O_4$/NF, and $Fe_xCo_{2-x}P$/NF electrodes.

shows higher HER catalytic activity for the $Fe_xCo_{2-x}P$/NF electrode. Figure 6d demonstrates the multi-potential step curves of the prepared materials taken in the potential range −0.475 to 0.225 V (vs. RHE), with an increment of −0.1 V per 200 s. The current rises slowly with the potential, and remains nearly constant for a duration of 200 s. This assessment demonstrates better mass-transport property and conductivity, and the mechanical sturdiness of the electrode materials. The long-term stability of the electrocatalysts was evaluated using CP technique at a high current density of 50 mA cm^{-2} for a duration of 30 h (Figure 6e). Figure 6e shows low stability for FeCo-PBA/NF, whereas $Fe_xCo_{3-x}O_4$/NF maintains almost the same potential as the initial one. However, $Fe_xCo_{2-x}P$/NF shows low potential and maintains stable potential compared to the other two, signifying excellent HER catalytic activity and stability over a long period (30 h). The polarization curve of $Fe_xCo_{2-x}P$/NF after the CP stability test is almost identical to the initial one (Figure S15a). Thus, $Fe_xCo_{2-x}P$/NF shows excellent HER performance compared to $Fe_xCo_{3-x}O_4$/NF and FeCo-PBA/NF in the alkaline medium. Further, the HER activity of $Fe_xCo_{2-x}P$/NF in the presence of urea is also evaluated by using 1 M KOH + 0.5 M urea as the electrolyte. The LSV curve of $Fe_xCo_{2-x}P$/NF-urea in Figure 6a shows that the presence of urea does not have a substantial impact on the HER activity of $Fe_xCo_{2-x}P$/NF, it shows only a small decrease in the potential after 100 mA cm^{-2}. For the urea-containing electrolyte, $Fe_xCo_{2-x}P$/NF-urea requires an overpotential of 122 mV at the current density of 10 mA cm^{-2}, and 177 mV at 50 mA cm^{-2}. Further, the HER electrocatalytic activity trend of the electrocatalysts in both the cases (electrolyte with and without urea) with respect to mass loading and ECSA is also determined by normalizing the respective LSV curves with their corresponding mass loadings and ECSA values, which are shown in Figure S16a, b. In both cases, the electrocatalytic activity trend is similar to that of Figure 6a. The corresponding derived Tafel slope of $Fe_xCo_{2-x}P$/NF in the presence of urea, with respect to LSV profiles in Figure 6a is 95 mV dec^{-1}, which is almost the same as that of $Fe_xCo_{2-x}P$/NF (97 mV dec^{-1}) without urea. The CP stability curve of $Fe_xCo_{2-x}P$/NF-urea in Figure 6e shows an insignificant change in the potential for 30 h at a current density of 50 mA cm^{-2}. Thus, the presence of urea has little influence on the HER activity of $Fe_xCo_{2-x}P$/NF. Therefore, $Fe_xCo_{2-x}P$/NF is a better-suited electrode to use in KOH, and KOH + urea electrolytes to perform UOR/OER and HER.

From the above observations, it is found that $Fe_xCo_{2-x}P$/NF exhibits the highest catalytic activity for OER, UOR, and HER compared with $Fe_xCo_{3-x}O_4$/NF despite the similar morphological features and the metal ions. This can be attributed to the following factors: (i) during OER in alkaline media, transition metal phosphides undergo in situ partial oxidation at the surface and form hydroxide/oxyhydroxide phase, which is highly active phase for remarkable OER catalytic activity,[70] the phosphide materials are good electrical conductors that remain at the core, and the phosphide and hydroxide interface acts as bridge for better carrier transportation from the core phosphide to the outer hydroxide surface; (ii) in the HER case, the presence of low electronegative P species in transition metal phosphides helps in trapping protons and easy hydrogen desorption process;[71,72] (iii) the existence of individually highly catalytically active Co_2P and Fe_2P phases in a single $Fe_xCo_{2-x}P$/NF material is more beneficial in terms of increasing the number of active sites and altering their electronic properties for exhibiting high conductivity;[73,74] (iv) the presence of N-C matrix acts as a protective layer that prevents the dissolution of the electrocatalytically active materials and is also advantageous in improving the conductivity of the material;[75,76] and (v) the higher SSA of $Fe_xCo_{2-x}P$/NF material compared to the other two also facilitates the catalytic activity owing to better exposure of the catalytically active sites. Therefore, because of the synergistic effect, $Fe_xCo_{2-x}P$/NF shows excellent bifunctional catalytic activity and stability.

Overall water splitting study

Based on the above three-electrode electrochemical results for OER/UOR and HER, it can be clearly observed that $Fe_xCo_{2-x}P$/NF can effectively function as both anode and cathode. Figure 7a shows the cell potentials ($E_{cell} = E_{anode} + E_{cathode}$) that are evaluated from the half-cell anodic and cathodic potentials. The hollow structured $Fe_xCo_{2-x}P$/NF requires a potential of

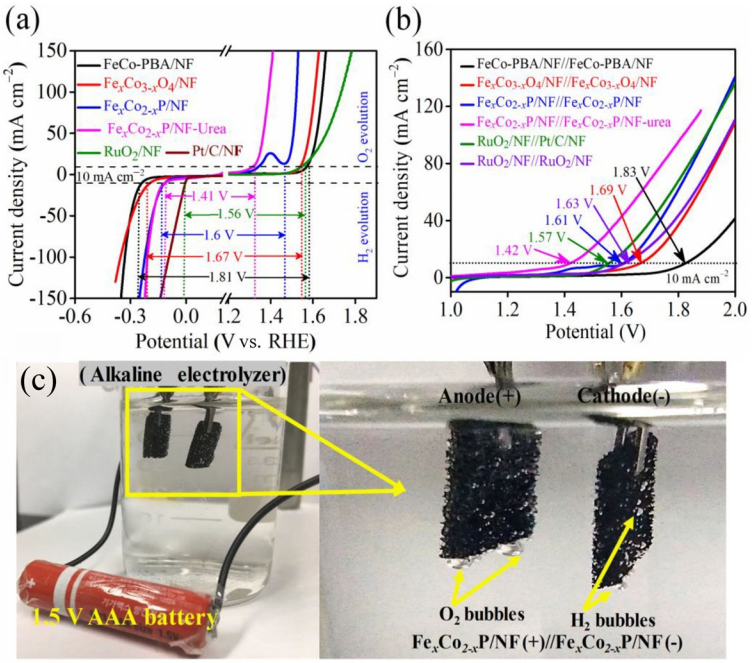

Figure 7. (a) Cell potential determination from *iR*-corrected LSV curves of OER/UOR and HER of FeCo-PBA/NF, $Fe_xCo_{3-x}O_4$/NF, and $Fe_xCo_{2-x}P$/NF electrodes materials at a scan rate of 2 mV s^{-1}, (b) LSV curves of FeCo-PBA/NF(+) || FeCo-PBA/NF(−), $Fe_xCo_{3-x}O_4$/NF(+) || $Fe_xCo_{3-x}O_4$/NF(−), and $Fe_xCo_{2-x}P$/NF(+) || $Fe_xCo_{2-x}P$/NF(−) electrolyzers in comparison with electrolyzers constructed from the state-of-the-art electrocatalysts RuO_2/NF(+) || Pt/C/NF(−) and RuO_2/NF(+) || RuO_2/NF(−), and (c) optical image of $Fe_xCo_{2-x}P$/NF(+) || $Fe_xCo_{2-x}P$/NF(−) electrolyzer driven by a 1.5 V AAA battery generating O_2 and H_2 gas bubbles at anode and cathode in 1.0 M KOH electrolyte, respectively.

only 1.6 V to drive a current density of 10 mA cm^{-2}, whereas $Fe_xCo_{3-x}O_4$/NF and FeCo-PBA/NF need 1.67 and 1.81 V, respectively. Interestingly, when UOR replaces OER, $Fe_xCo_{2-x}P$/NF takes only 1.41 V to drive 10 mA cm^{-2}, which is extremely promising. However, it is essential to study the real performance of the electrodes for overall water splitting in the two-electrode configuration electrolytic cell, so that they can be accounted for practical applications. To test the efficiency of $Fe_xCo_{2-x}P$/NF for overall water splitting, $Fe_xCo_{2-x}P$/NF(+) || $Fe_xCo_{2-x}P$/NF(−) alkaline electrolyzer is constructed, utilizing it as anode and cathode. For comparison, $Fe_xCo_{3-x}O_4$/NF(+) || $Fe_xCo_{3-x}O_4$/NF(−) and FeCo-PBA/NF(+) || FeCo-PBA/NF(−) electrolyzers are also constructed, along with the state-of-the-art-electrocatalyst-based electrolyzers, such as RuO_2/NF(+) || Pt/C/NF(−) and RuO_2/NF(+) || RuO_2/NF(−). Figure 7b shows the LSV curves of the constructed electrolyzers. The $Fe_xCo_{2-x}P$/NF-based electrolyzer demonstrates excellent overall water splitting performance with a cell potential of 1.61 V at the current density of 10 mA cm^{-2}, which is lower than those of $Fe_xCo_{3-x}O_4$/NF (1.69 V) and FeCo-PBA/NF-based (1.83 V) electrolyzers. The cell potential (E_{cell}) of the $Fe_xCo_{2-x}P$/NF-based electrolyzer is lower than many of the recently investigated electrolyzers, and Table S4 shows the relevant comparison. In addition, the overall electrochemical water splitting activity of $Fe_xCo_{2-x}P$/NF(+) || $Fe_xCo_{2-x}P$/NF(−) alkaline electrolyzer is tested using a 1.5 V AAA battery. Figure 7c shows that the O_2 and H_2 gas bubbles generated using the 1.5 V battery is clearly visible at the anode and cathode of the electrolyzer. Finally, the overall water splitting performance of $Fe_xCo_{2-x}P$/NF-based electrolyzer is investigated in the presence of urea (0.5 M), and Figure 7b shows the corresponding LSV curve (labelled as $Fe_xCo_{2-x}P$/NF//$Fe_xCo_{2-x}P$/NF-urea). Impressively when urea is used, the cell-potential of $Fe_xCo_{2-x}P$/NF(+) || $Fe_xCo_{2-x}P$/NF(−) alkaline electrolyzer is greatly reduced by 0.19 V, demanding only 1.42 V to drive a current density of 10 mA cm^{-2}. The cell potentials obtained in the presence and absence of urea for $Fe_xCo_{2-x}P$/NF-based electrolyzer at 10 mA cm^{-2} in the two-electrode system are much less than the previously reported values of other electrolyzers (Table S4). These results unambiguously show that $Fe_xCo_{2-x}P$/NF can be used as a highly efficient bifunctional electrocatalyst in alkaline electrolysis and urea-based electrolysis for overall water splitting.

Post-physical characterizations

During the long term OER/UOR and HER stability tests, electrocatalysts are often found to undergo certain morphological as well as structural changes that can significantly affect their electrochemical performances, especially metal phosphides that undergo interfacial oxidation under the electrochemical oxidation conditions, such as OER and UOR.[70,77] In the present work also, $Fe_xCo_{2-x}P$/NF is expected to undergo such interfacial oxidation during OER and UOR stability tests. Therefore, to identify any such structural changes, PXRD patterns of $Fe_xCo_{2-x}P$/NF after OER, UOR, and HER were recorded and are shown in Figure S17a. However, the diffraction patterns of $Fe_xCo_{2-x}P$/NF after OER, UOR, and HER stability tests are all found to be identical to that of the initial one (Figure 1a). Similarly, the PXRD patterns of $Fe_xCo_{3-x}O_4$/NF after OER and HER stability tests (Figure S17b) do not show any changes, indicating that there is no considerable change in the phase of the materials; however, PXRD is insensitive to small interfacial changes. Therefore, to critically examine the changes in the near-surface chemical compositions and the oxidation states of the constituents of the electrocatalysts, XPS was recorded for the electrocatalysts after OER/UOR and HER stability tests. The XPS spectra of $Fe_xCo_{2-x}P$/NF recorded after OER and UOR stability tests are shown in Figure S18 and S19, respectively. The survey spectra of $Fe_xCo_{2-x}P$/NF (Figure S18a and S19a) show the presence of the constituent elements. However, it is interesting to note that the intensity of the O 1s peak is increased greatly after OER and UOR stability tests compared to that of the initial survey spectrum (shown in Figure 4a), whereas the intensity of P 2p is reduced indicating the clear evidence of surface oxidation. Further analysis of the Co 2p XPS spectrum of $Fe_xCo_{2-x}P$/NF after OER shows two peaks at the binding energy of 780.6 and 795.8 eV, which can be attributed to the oxidized cobalt species, whereas the peak at 782.7 eV can be assigned to cobalt hydroxo species (Figure S18b).[78] Also, the Fe 2p spectrum shows peaks at 712.9 and 724.4 eV that can be attributed to oxidized Fe species (Figure S18c).[78] The deconvoluted O 1s spectrum also shows a typical contribution of metal-oxides/hydroxides contribution, which is manifested at the binding energy of 530.3 eV with a more dominant contribution of a typical interfacial hydroxyl species at the binding energy of 531.8 eV (Figure S18e).[78] The peak at 533.9 eV may correspond to the C–O bonds.[78] The deconvoluted P 2p XPS spectrum (Figure S18d) also shows dominant peaks at 132.9, 134.1, and 135.5 eV, corresponding to phosphate species,[65] whereas the phosphide peak that was initially observed at a binding energy of approximately 129 eV before OER stability test (Figure 4d) completely disappeared after the OER stability test, suggesting that the phosphide near the surface of the electrocatalyst underwent in situ oxidation. Such similar trends in the binding energies of Co 2p, Fe 2p, O 1s, and P 2p were also found in the case of $Fe_xCo_{2-x}P$/NF after UOR stability test (Figure S19b–e), which implies that similar surface oxidation has occurred under UOR condition as well. These findings demonstrate that there was rearrangement of surface during electrochemical oxidation conditions of OER and UOR. Therefore, the true catalytic nature of the $Fe_xCo_{2-x}P$/NF electrocatalysts can be considered to originate from the combined effect of the synergistic nature of Fe–Co oxo/hydroxo species and phosphate species, which accounted for its excellent OER/UOR performance.

The FESEM images of $Fe_xCo_{2-x}P$/NF samples recorded after OER and UOR stability tests are shown in Figure S20a and S20b, respectively. These images show that the initial morphology is maintained even after the long term OER and UOR stability tests. Similarly, $Fe_xCo_{3-x}O_4$/NF electrocatalyst after OER and HER does not show any significant morphological changes (Figure S21a, b). However, the morphology of the FeCo-PBA/NF electrocatalysts after long term OER and HER stability tests is completely changed to sheet-like structures (Figure S22a, b).

Similarly, the internal structure of the electrocatalysts after long term OER/UOR stability tests are also investigated using HRTEM technique. TEM images of $Fe_xCo_{2-x}P$/NF electrocatalysts after OER and UOR stability tests also show almost the similar internal structure as that of the initial ones indicating its structural robustness (Figures S23 and S24). Likewise, $Fe_xCo_{3-x}O_4$/NF also exhibits similar internal structural robustness after the long term OER stability test (Figure S25). However, TEM images of FeCo-PBA/NF show the complete decomposition of the initial structure to sheet-like structures after long term OER stability test (Figure S26), in agreement with that of the FESEM observation (Figure S22 a). This indicates that FeCo-PBA/NF is not a stable and suitable electrocatalyst compared to its derivatives ($Fe_xCo_{3-x}O_4$/NF and $Fe_xCo_{2-x}P$/NF), which is also in good agreement with the electrochemical results discussed above. Thus, the post-physical characterizations of the electrocatalysts adequately support their electrochemical results.

Conclusion

We derived Prussian blue analogue (FeCo-PBA), $Fe_xCo_{2-x}P$, $Fe_xCo_{3-x}O_4$ microbuilding arrays on Ni foam (NF) using a Co-based metal–organic frameworks (Co-MOF)/NF as starting material through a simple solid–liquid, solid–solid, and solid–gas anion-exchange reaction, respectively. A facile room temperature (RT) and post-heat treatment route is employed for Fe-incorporation and anion exchange, which is also optimized by varying the Fe-precursor concentration and reaction time. The hollow-structured $Fe_xCo_{2-x}P$/NF material containing N-doped carbon (N-C) exhibits high conductivity, and abundant catalytically active sites, which results in excellent oxygen evolution reaction (OER)/urea oxidation reaction (UOR), hydrogen evolution reaction (HER), and overall water splitting performance, compared with $Fe_xCo_{3-x}O_4$/NF and FeCo-PBA/NF. A two-electrode alkaline electrolyzer comprising $Fe_xCo_{2-x}P$/NF as anode and cathode deliver a current density of 10 mA cm^{-2} at a cell potential of just 1.61 V, and when it is externally connected to a 1.5 V AAA battery, the H_2 and O_2 gas bubbles are generated, and liberation occurs rapidly. The overall water splitting performance follows the order $Fe_xCo_{2-x}P$/NF(+) || $Fe_xCo_{2-x}P$/NF(−) > $Fe_xCo_{3-x}O_4$/NF(+) || $Fe_xCo_{3-x}O_4$/NF(−) > FeCo-PBA/NF(+) || FeCo-PBA/NF(−). The same electrolyzer with $Fe_xCo_{2-x}P$/NF (±) is used for the urea electrolysis by changing the electrolyte to 1 M KOH + 0.5 M urea. Impressively, the urea electrolysis cell potential is reduced to 1.42 from 1.61 V of water electrolysis to achieve a current density of 10 mA cm^{-2}. Thus, urea electrolysis with the $Fe_xCo_{2-x}P$/NF-based electrolyzer produces green H_2 fuel at low cell potential, and it treats urea-rich wastewater. Therefore, our study paves the way for the design and synthesis of highly efficient bifunctional MOF-derived electrocatalysts by a simple synthesis route. This synthesis strategy is expected to broaden the utilization of MOFs precursors, to develop high-efficiency electrode materials for numerous energy storage and conversion applications.

Experimental Section

Synthesis of Co-MOF/NF

Initially, NF (2 cm × 4 cm) was cleaned by sonicating for 15 min in 3 M HCl aqueous solution, followed by washing with deionized (DI) water and acetone, respectively. After that, Co aqueous solution and 2–methylimidazole aqueous solutions were prepared separately by dissolving 1 mmol of cobalt nitrate hexahydrate and 16 mmol of 2–methylimidazole in 40 mL DI water, respectively. These two solutions were then mixed and magnetically stirred for 1 min. Then, the pre-cleaned NF was submerged into the mixed solution and kept for 12 h at RT (27 °C), without any disturbance. Finally, the Co-MOF grown NF (Co-MOF/NF) was collected, washed with DI water several times, and kept in an electric oven at 60 °C for 8 h to dry.

Synthesis of FeCo-PBA/NF

A piece of pre-synthesized Co-MOF/NF (2 cm × 4 cm) was soaked in an aqueous potassium hexacyanoferrate(III) solution ($K_3[Fe(CN)_6]$), at which stage the purple color of the Co-MOF/NF changed to dark green, indicating the formation of FeCo-PBA/NF owing to anion exchange reaction. To optimize the concentration of potassium hexacyanoferrate and reaction time, we prepared three different concentrations of solutions by dissolving hexacyanoferrate (0.25, 0.5, and 1 mmol) in DI water (50 mL), and aged at RT for a duration of 12 and 24 h. The aging time of 12 h and 0.5 mmol concentration of potassium hexacyanoferrate were found to be the optimum conditions; therefore, FeCo-PBA/NF synthesized under the optimized conditions was washed with DI water and ethanol several times, and dried at 60 °C.

Synthesis of $Fe_xCo_{2-x}P$/NF

$Fe_xCo_{2-x}P$/NF was obtained through phosphorization under heat treatment in an Ar atmosphere. Typically, sodium hypophosphate (1 g) was taken in a quartz boat and placed 2 cm ahead of another boat containing a piece of FeCo-PBA/NF inside a furnace tube along the forward direction of the gas flow. The temperature was initially raised to 400 °C at the slow heating rate of 1 °C min^{-1}, and then maintained at 400 °C for 2 h, with the Ar gas flow at 500 sccm. Finally, it was allowed to naturally cool down to RT.

Synthesis of $Fe_xCo_{3-x}O_4$/NF

$Fe_xCo_{3-x}O_4$/NF was obtained by heating FeCo-PBA/NF at 350 °C in an air atmosphere for 2 h at a slow heating rate of 1 °C min^{-1}.

Material characterization

The phase and structure of Co-MOF/NF, FeCo-PBA/NF, $Fe_xCo_{3-x}O_4$/NF, and $Fe_xCo_{2-x}P$/NF were studied by using PXRD (Rigaku Corporation, Japan, CuK_α radiation, wavelength $\lambda = 0.154$ nm) in the 2θ range of 10–80° at a scan rate of 3° min^{-1}. FTIR spectroscopy was utilized to investigate the available surface functional groups and the types of bonding using Nicolet 6700 spectrometry (Thermo Scientific, USA). TGA was performed by using a Q50 TGA (TA Instruments, New Castle, US). The morphology, structure, and elemental composition were examined by FESEM (JSM-6701F; JEOL, Japan), HRTEM, STEM (JEM-2200 FS; JEOL Ltd., Japan, 200 kV), and EDX. Valence states of the elements and surface chemical compositions of the samples were investigated by XPS (Theta Probe; Thermo Fisher

Scientific, UK). The multipoint nitrogen adsorption–desorption experiment was performed on ASAP 2020 Plus system (Micromeritics Instrument Corp.,USA) analyzer. Before the physisorption measurement, all the samples were degassed at 100 °C for 12 h with the help of a dynamic vacuum. The SSA of the materials were determined using BET gas adsorption method, at 77 K and the pore size distribution profiles were obtained from the adsorption branch of the isotherm using the BJH method.

Electrochemical characterizations

The electrocatalytic activities of FeCo-PBA/NF, $Fe_xCo_{3-x}O_4$/NF, and $Fe_xCo_{2-x}P$/NF for OER, HER, and overall water splitting were studied on a CHI 660E electrochemical workstation using three electrodes (for OER/UOR and HER) and a two-electrode system (for overall water splitting and urea electrolysis). The 1 cm^2 area of NF deposited with FeCo-PBA/NF, $Fe_xCo_{3-x}O_4$/NF, and $Fe_xCo_{2-x}P$/NF (mass loading $\approx$4 mg cm^{-2}) were used directly as working electrodes. A graphite rod and Ag/AgCl (saturated KCl) were used as counter and reference electrodes, respectively. Freshly prepared aqueous 1.0 M KOH and 1.0 M KOH containing 0.5 M urea solutions were used separately as electrolytes for water electrolysis and urea electrolysis, respectively. Electrochemical impedance spectroscopy (EIS) measurements were obtained by supplying an AC voltage of amplitude 5 mV in the frequency range (0.01 Hz–100 kHz). All the potentials, if not specifically mentioned, were changed to RHE using the Nernst equation ($E_{RHE} = E_{Ag/AgCl} + 0.059 \times pH + 0.197$). The LSV curves were i$R$-corrected by using the equation $E_{corr} = E_{mea} - iR_c$, where R_c is the corrected resistance, E_{mea} is the potential measured experimentally, and E_{corr} is the iR-corrected potential. The η values for water electrolysis were obtained from the equation $\eta = E_{RHE} - 1.23$ V. For comparison, commercial Pt/C (20 wt%) and RuO_2 (99.9 wt%, Alfa) were loaded on a 1 cm^2 area of pre-cleaned NF. The catalyst's inks were made by dispersing Pt/C and RuO_2 (5 mg) separately in a solution mixture of isopropyl alcohol (750 μL), DI water (200 μL), and nafion (50 μL) for 30 min under ultrasonication.

Acknowledgements

The authors acknowledge the financial support from the Basic Research Program (Grant No. 2017R1A2B3004917) through National Research Foundation (NRF), sponsored by Ministry of Science, ICT & Future Planning of the Republic of Korea.

Conflict of interest

The authors declare no conflict of interest.

Keywords: bifunctional electrode · hollow structures · metal–organic frameworks · urea electrolysis · water electrolysis

[1] J. A. Turner, *Science* **2004**, *305*, 972.
[2] H. B. Gray, *Nat. Chem.* **2009**, *1*, 7.
[3] Y. Jiao, Y. Zheng, M. Jaroniec, S. Z. Qiao, *Chem. Soc. Rev.* **2015**, *44*, 2060.
[4] N. Cheng, S. Stambula, D. Wang, M. N. Banis, J. Liu, A. Riese, B. Xiao, R. Li, T. K. Sham, L. M. Liu, G. A. Botton, X. Sun, *Nat. Commun.* **2016**, *7*, 13638.
[5] G. Rajeshkhanna, T. I. Singh, N. H. Kim, J. H. Lee, *ACS Appl. Mater. Interfaces* **2018**, *10*, 42453.
[6] Y. Yang, L. Dang, M. J. Shearer, H. Sheng, W. Li, J. Chen, P. Xiao, Y. Zhang, R. J. Hamers, S. Jin, *Adv. Energy Mater.* **2018**, *8*, 1703189.
[7] M. S. Burke, S. Zou, L. J. Enman, J. E. Kellon, C. A. Gabor, E. Pledger, S. W. Boettcher, *J. Phys. Chem. Lett.* **2015**, *6*, 3737.
[8] Y. Pi, Q. Shao, P. Wang, F. Lv, S. Guo, J. Guo, X. Huang, *Angew. Chem. Int. Ed.* **2017**, *56*, 4502; *Angew. Chem.* **2017**, *129*, 4573.
[9] M. W. Louie, A. T. Bell, *J. Am. Chem. Soc.* **2013**, *135*, 12329.
[10] F. Song, L. Bai, A. Moysiadou, S. Lee, C. Hu, L. Liardet, X. Hu, *J. Am. Chem. Soc.* **2018**, *140*, 7748.
[11] G. Ou, F. Wu, K. Huang, N. Hussain, D. Zu, H. Wei, B. Ge, H. Yao, L. Liu, H. Li, Y. Shi, H. Wu, *ACS Appl. Mater. Interfaces* **2019**, *11*, 3978.
[12] G. Ou, P. Fan, H. Zhang, K. Huang, C. Yang, W. Yu, H. Wei, M. Zhong, H. Wu, Y. Li, *Nano Energy* **2017**, *35*, 207.
[13] G. Ou, C. Yang, Y. Liang, N. Hussain, B. Ge, K. Huang, Y. Xu, H. Wei, R. Zhang, H. Wu, *Small Methods* **2019**, *3*, 1800279.
[14] K. Liu, C. Zhang, Y. Sun, G. Zhang, X. Shen, F. Zou, H. Zhang, Z. Wu, E. C. Wegener, C. J. Taubert, J. T. Miller, Z. Peng, Y. Zhu, *ACS Nano* **2018**, *12*, 158.
[15] D. H. Ha, B. Han, M. Risch, L. Giordano, K. P. C. Yao, P. Karayaylali, Y. Shao-Horn, *Nano Energy* **2016**, *29*, 37.
[16] G. Rajeshkhanna, S. Kandula, K. R. Shrestha, N. H. Kim, J. H. Lee, *Small* **2018**, *14*, 1803638.
[17] A. P. Tiwari, D. Kim, Y. Kim, O. Prakash, H. Lee, *Nano Energy* **2016**, *28*, 366.
[18] L. Guo, L. Ji, J. Wang, S. Zuo, Z. Chen, *ACS Appl. Mater. Interfaces* **2018**, *10*, 36824.
[19] Y.-J. Ko, J.-M. Cho, I. Kim, D. S. Jeong, K.-S. Lee, J.-K. Park, Y.-J. Baik, H.-J. Choi, W.-S. Lee, *Appl. Catal. B* **2017**, *203*, 684.
[20] X. Zhao, B. Pattengale, D. Fan, Z. Zou, Y. Zhao, J. Du, J. Huang, C. Xu, *ACS Energy Lett.* **2018**, *3*, 2520.
[21] X. Wang, L. Yu, B. Y. Guan, S. Song, X. W. D. Lou, *Adv. Mater.* **2018**, *30*, 1801211.
[22] P. Cai, J. Huang, J. Chen, Z. Wen, *Angew. Chem. Int. Ed.* **2017**, *56*, 4858; *Angew. Chem.* **2017**, *129*, 4936.
[23] F. Ming, H. Liang, H. Shi, X. Xu, G. Mei, Z. Wang, *J. Mater. Chem. A* **2016**, *4*, 15148.
[24] T. Zhang, J. Du, P. Xi, C. Xu, *ACS Appl. Mater. Interfaces* **2017**, *9*, 362.
[25] Z. F. Huang, J. Song, K. Li, M. Tahir, Y. T. Wang, L. Pan, L. Wang, X. Zhang, J. J. Zou, *J. Am. Chem. Soc.* **2016**, *138*, 1359.
[26] Y. Li, J. Liu, C. Chen, X. Zhang, J. Chen, *ACS Appl. Mater. Interfaces* **2017**, *9*, 5982.
[27] J. Chen, J. Liu, J.-Q. Xie, H. Ye, X.-Z. Fu, R. Sun, C.-P. Wong, *Nano Energy* **2019**, *56*, 225.
[28] C. Tang, R. Zhang, W. Lu, L. He, X. Jiang, A. M. Asiri, X. Sun, *Adv. Mater.* **2017**, *29*, 1602441.
[29] Y. Li, H. Wang, Y. Li, Q. Wang, D. Li, R. Wang, B. He, Y. Gong, *J. Catal.* **2018**, *364*, 48.
[30] G. Zhong, D. Liu, J. Zhang, *J. Mater. Chem. A* **2018**, *6*, 1887 – 1899.
[31] J. Wang, W. Cui, Q. Liu, Z. Xing, A. M. Asiri, X. Sun, *Adv. Mater.* **2016**, *28*, 215.
[32] M. W. Kanan, Y. Surendranath, D. G. Nocera, *Chem. Soc. Rev.* **2009**, *38*, 109.
[33] G. Rajeshkhanna, G. R. Rao, *Int. J. Hydrogen Energy* **2018**, *43*, 4706.
[34] Y. Pei, Y. Cheng, J. Chen, W. Smith, P. Dong, P. M. Ajayan, M. Ye, J. Shen, *J. Mater. Chem. A* **2018**, *6*, 23220.
[35] F. Li, Y. Bu, Z. Lv, J. Mahmood, G. F. Han, I. Ahmad, G. Kim, Q. Zhong, J. B. Baek, *Small* **2017**, *13*, 1701167.
[36] Z. Cao, T. Zhou, W. Xi, Y. Zhao, *Electrochim. Acta* **2018**, *263*, 576.
[37] L. Zhang, H. B. Wu, X. W. D. Lou, *J. Am. Chem. Soc.* **2013**, *135*, 10664.
[38] H. Hu, B. Y. Guan, X. W. D. Lou, *Chem* **2016**, *1*, 102.
[39] B. Y. Guan, Y. Lu, Y. Wang, M. Wu, X. W. D. Lou, *Adv. Funct. Mater.* **2018**, *28*, 1706738.
[40] Y. Noori, K. Akhbari, *RSC Adv.* **2017**, *7*, 1782.
[41] Y. Han, J.-R. Li, Y. Xie, G. Guo, *Chem. Soc. Rev.* **2014**, *43*, 5952.
[42] E. Hu, J. Ning, D. Zhao, C. Xu, Y. Lin, Y. Zhong, Z. Zhang, Y. Wang, Y. Hu, *Small* **2018**, *14*, 1704233.
[43] B. K. Boggs, R. L. King, G. G. Botte, *Chem. Commun.* **2009**, 4859.
[44] Z.-Y. Yu, C.-C. Lang, M.-R. Gao, Y. Chen, Q.-Q. Fu, Y. Duan, S.-H. Yu, *Energy Environ. Sci.* **2018**, *11*, 1890.
[45] F. Wu, G. Ou, J. Yang, H. Li, Y. Gao, F. Chen, Y. Wang, Y. Shi, *Chem. Commun.* **2019**, *55*, 6555.
[46] F. Wu, G. Ou, Y. Wang, H. Zhong, L. Zhang, H. Li, Y. Shi, *Chem. Asian J.* **2019**, *14*, 2796.

[47] Y. Xu, B. Zhang, *ChemElectroChem* **2019**, *6*, 3214.
[48] Y. Huang, X. Chong, C. Liu, Y. Liang, B. Zhang, *Angew. Chem. Int. Ed.* **2018**, *57*, 13163; *Angew. Chem.* **2018**, *130*, 13347.
[49] Y. Wang, Y. Yu, R. Jia, C. Zhang, B. Zhang, *Natl. Sci. Rev.* **2019**, *6*, 730 .
[50] C. Huang, Y. Huang, C. Liu, Y. Yu, B. Zhang, *Angew. Chem. Int. Ed.* **2019**, *58*, 12014; *Angew. Chem.* **2019**, *131*, 12142.
[51] S. Shen, M. Li, B. Li, Z. Zhao, *Environ. Sci. Pollut. Res.* **2014**, *21*, 12563.
[52] M. von Ahnen, L.-F. Pedersen, P. B. Pedersen, J. Dalsgaard, *Aquacultural Eng.* **2015**, *69*, 50.
[53] A. Lundström, T. Snelling, P. Morsing, P. Gabrielsson, E. Senar, L. Olsson, *Appl. Catal. B* **2011**, *106*, 273.
[54] C. Xue, L. D. Wilson, *Carbohydr. Polym.* **2016**, *135*, 180.
[55] Y. Ma, J. He, Z. Kou, A. M. Elshahawy, Y. Hu, C. Guan, X. Li, J. Wang, *Adv. Mater. Interfaces* **2018**, *5*, 1800222.
[56] H. Fu, Z. Wang, X. Wang, P. Wang, C. C. Wang, *CrystEngComm* **2018**, *20*, 1473.
[57] Y. Zhang, Y. Jia, M. Li, L. Hou, *Sci. Rep.* **2018**, *8*, 9597.
[58] Y. Hu, H. Kazemian, S. Rohani, Y. Huang, Y. Song, *Chem. Commun.* **2011**, *47*, 12694.
[59] N. Wang, W. Ma, Z. Ren, Y. Du, P. Xu, X. Han, *J. Mater. Chem. A* **2018**, *6*, 884.
[60] Y. Zhang, L. Gao, E. J. M. Hensen, J. P. Hofmann, *ACS Energy Lett.* **2018**, *3*, 1360.
[61] H. Liang, A. N. Gandi, D. H. Anjum, X. Wang, U. Schwingenschlögl, H. N. Alshareef, *Nano Lett.* **2016**, *16*, 7718.
[62] C. Tang, L. Gan, R. Zhang, W. Lu, X. Jiang, A. M. Asiri, X. Sun, J. Wang, L. Chen, *Nano Lett.* **2016**, *16*, 6617.
[63] B. Owens-Baird, Y. V. Kolen'ko, K. Kovnir, *Chem. Eur. J.* **2018**, *24*, 7298.
[64] J. Hao, W. Yang, Z. Zhang, J. Tang, *Nanoscale* **2015**, *7*, 11055.
[65] J. D. Wood, S. A. Wells, D. Jariwala, K.-S. Chen, E. Cho, V. K. Sangwan, X. Liu, L. J. Lauhon, T. J. Marks, M. C. Hersam, *Nano Lett.* **2014**, *14*, 6964.
[66] J. T. Titantah, D. Lamoen, *Diamond Relat. Mater.* **2007**, *16*, 581.
[67] Z. Wu, Z. Zou, J. Huang, F. Gao, *J. Catal.* **2018**, *358*, 243.
[68] T. Zhang, Z. Zhu, H. Chen, Y. Bai, S. Xiao, X. Zheng, Q. Xue, S. Yang, *Nanoscale* **2015**, *7*, 2933.
[69] C. Wei, S. Sun, D. Mandler, X. Wang, S. Z. Qiao, Z. J. Xu, *Chem. Soc. Rev.* **2019**, *48*, 2518.
[70] A. Dutta, N. Pradhan, *J. Phys. Chem. Lett.* **2017**, *8*, 144.
[71] J. Kibsgaard, C. Tsai, K. Chan, J. D. Benck, J. K. Nørskov, F. Abild-Pedersen, T. F. Jaramillo, *Energy Environ. Sci.* **2015**, *8*, 3022.
[72] R. B. Wexler, J. M. P. Martirez, A. M. Rappe, *ACS Catal.* **2017**, *7*, 7718.
[73] A. Dutta, A. K. Samantara, S. K. Dutta, B. K. Jena, N. Pradhan, *ACS Energy Lett.* **2016**, *1*, 169.
[74] D. E. Schipper, Z. Zhao, H. Thirumalai, A. P. Leitner, S. L. Donaldson, A. Kumar, F. Qin, Z. Wang, L. C. Grabow, J. Bao, K. H. Whitmire, *Chem. Mater.* **2018**, *30*, 3588.
[75] Y. Bai, H. Zhang, Y. Feng, L. Fang, Y. Wang, *J. Mater. Chem. A* **2016**, *4*, 9072.
[76] J. Yu, Q. Li, N. Chen, C. Y. Xu, L. Zhen, J. Wu, V. P. Dravid, *ACS Appl. Mater. Interfaces* **2016**, *8*, 27850.
[77] J. Yang, H. Liu, W. N. Martens, R. L. Frost, *J. Phys. Chem. C* **2010**, *114*, 111.
[78] M. C. Biesinger, B. P. Payne, A. P. Grosvenor, L. W. M. Lau, A. R. Gerson, R. S. C. Smart, *Appl. Surf. Sci.* **2011**, *257*, 2717.

Manuscript received: August 17, 2019
Revised manuscript received: September 18, 2019
Version of record online: October 15, 2019